The Astrophysical Journal Letters, 970:L40 (15pp), 2024 August 1 https://doi.org/10.3847/2041-8213/ad6144

Direct Observational Evidence of Multi-epoch Massive Star Formation in G24.47+0.49

Anindya Saha[1], Anandmayee Tej[1], Hong-Li Liu[2], Tie Liu[3,4], Guido Garay[5], Paul F. Goldsmith[6], Chang Won Lee[7,8], Jinhua He[5,9,10], Mika Juvela[11], Leonardo Bronfman[5], Tapas Baug[12], Enrique Vázquez-Semadeni[13], Patricio Sanhueza[14,15], Shanghuo Li[16], James O. Chibueze[17,18], N. K. Bhadari[19], Lokesh K. Dewangan[19], Swagat Ranjan Das[5], Feng-Wei Xu[20,21,22], Namitha Issac[3], Jihye Hwang[8], and L. Viktor Tóth[23,24]

[1] Indian Institute of Space Science and Technology, Thiruvananthapuram 695 547, Kerala, India; anindya.s1130@gmail.com, tej@iist.ac.in
[2] Department of Astronomy, Yunnan University, Kunming, 650091, People's Republic of China; hongliliu2012@gmail.com
[3] Shanghai Astronomical Observatory, Chinese Academy of Sciences, 80 Nandan Road, Shanghai 200030, People's Republic of China
[4] Key Laboratory for Research in Galaxies and Cosmology, Shanghai Astronomical Observatory, Chinese Academy of Sciences, 80 Nandan Road, Shanghai 200030, People's Republic of China
[5] Departamento de Astronomía, Universidad de Chile, Las Condes, Santiago 7550000, Chile
[6] Jet Propulsion Laboratory, California Institute of Technology, 4800 Oak Grove Drive, Pasadena, CA 91109, USA
[7] University of Science and Technology, Korea (UST), 217 Gajeong-ro, Yuseong-gu, Daejeon 34113, Republic of Korea
[8] Korea Astronomy and Space Science Institute, 776 Daedeokdae-ro, Yuseong-gu, Daejeon 34055, Republic of Korea
[9] Yunnan Observatories, Chinese Academy of Sciences, Phoenix Mountain, East Suburb of Kunming, 650216, Yunnan, People's Republic of China
[10] Chinese Academy of Sciences, South America Center for Astrophysics (CASSACA) at Cerro Calán, Camino El Observatorio #1515, Las Condes, Santiago, Chile
[11] Department of Physics, P.O. Box 64, FI- 00014, University of Helsinki, Finland
[12] Satyendra Nath Bose National Centre for Basic Sciences, Block-JD, Sector-III, Salt Lake, Kolkata-700 106, India
[13] Instituto de Radioastronomía y Astrofísica, Universidad Nacional Autónoma de México, Antigua Carretera a Pátzcuaro 8701, Ex-Hda. San José de la Huerta, 58089 Morelia, Michoacán, México
[14] National Astronomical Observatory of Japan, National Institutes of Natural Sciences, 2-21-1 Osawa, Mitaka, Tokyo 181-8588, Japan
[15] Astronomical Science Program, The Graduate University for Advanced Studies, SOKENDAI, 2-21-1 Osawa, Mitaka, Tokyo 181-8588, Japan
[16] Max Planck Institute for Astronomy, Königstuhl 17, D-69117 Heidelberg, Germany
[17] Department of Mathematical Sciences, University of South Africa, Cnr Christian de Wet Rd and Pioneer Avenue, Florida Park, 1709, Roodepoort, South Africa
[18] Department of Physics and Astronomy, Faculty of Physical Sciences, University of Nigeria, Carver Building, 1 University Road, Nsukka 410001, Nigeria
[19] Physical Research Laboratory, Navrangpura, Ahmedabad 380009, India
[20] Kavli Institute for Astronomy and Astrophysics, Peking University, Beijing 100871, People's Republic of China
[21] Department of Astronomy, School of Physics, Peking University, Beijing, 100871, People's Republic of China
[22] I. Physikalisches Institut, Universität zu Köln, Zülpicher Str. 77, D-50937 Köln, Germany
[23] Institute of Physics and Astronomy, Eötvös Loránd University, Pázmány Péter sétány 1/A, H-1117 Budapest, Hungary
[24] University of Debrecen, Institute of Physics, H-4026, Debrecen, Bem ter 18, Hungary
Received 2024 April 5; revised 2024 June 14; accepted 2024 June 29; published 2024 July 30

Abstract

Using new continuum and molecular line data from the Atacama Large Millimeter/submillimeter Array Three-millimeter Observations of Massive Star-forming Regions (ATOMS) survey and archival Very Large Array, 4.86 GHz data, we present direct observational evidence of hierarchical triggering relating three epochs of massive star formation in a ringlike H II region, G24.47+0.49. We find from radio flux analysis that it is excited by a massive star(s) of spectral type O8.5V–O8V from the first epoch of star formation. The swept-up ionized ring structure shows evidence of secondary collapse, and within this ring, a burst of massive star formation is observed in different evolutionary phases, which constitutes the second epoch. ATOMS spectral line (e.g., HCO^+(1–0)) observations reveal an outer concentric molecular gas ring expanding at a velocity of $\sim$9 km s^{-1}, constituting the direct and unambiguous detection of an expanding molecular ring. It harbors twelve dense molecular cores with surface mass density greater than 0.05 g cm^{-2}, a threshold typical of massive star formation. Half of them are found to be subvirial and thus in gravitational collapse making them the third epoch of potential massive star-forming sites.

Unified Astronomy Thesaurus concepts: Interstellar medium (847); Star formation (1569); Star forming regions (1565)

1. Introduction

Massive stars ($M_\star \gtrsim 8\,M_\odot$), with their powerful mechanical and radiative feedback, play a crucial role in regulating star formation within their natal environments. They can either initiate the formation of a subsequent generation of stars (e.g., Churchwell et al. 2006) or disperse the surrounding molecular gas, consequently inhibiting further star formation (e.g., Walch et al. 2012; Pabst et al. 2019; Bonne et al. 2023). H II regions and their role in triggered star formation has been in focus since the pioneering work by Elmegreen & Lada (1977). Over the last decade or so, there has been a plethora of observational evidence linking the expansion of H II regions to triggered star formation (e.g., Zavagno et al. 2006, 2007; Figueira et al. 2017, and references therein). The peripheries of infrared dust bubbles (Churchwell et al. 2006; Kendrew et al. 2012) have served as ideal sites to investigate triggered star formation through various competing mechanisms (e.g., Deharveng et al. 2010; Kendrew et al. 2012; Thompson et al. 2012; Liu et al. 2016; Das et al. 2017; Bhadari et al. 2021; Zhang et al. 2023b). However, theoretically (e.g., Dale et al. 2015; González-Samaniego & Vazquez-Semadeni 2020) and observationally

(e.g., Cambrésy et al. 2013), it is also seen that commonly used signposts of triggered star formation do not always lead to definite conclusions on positive feedback. Hence, these need to be cautiously interpreted to better constrain the impact of stellar feedback on triggering star formation.

These observational studies have offered a comprehensive insight into triggered star formation, connecting two generations of stars. In comparison, observational evidence for hierarchical triggering and multigeneration star formation is still scarce (e.g., Oey et al. 2005; Purcell et al. 2009; Areal et al. 2020). Oey et al. (2005) suggest a three-generation system of hierarchically triggered star formation in the W3/W4 complex, where expanding superbubbles and mechanical feedback from massive stars initiate later generations of star formation. Similarly, Purcell et al. (2009) report multigenerations of massive star formation in the NGC 3576, which is embedded in the center of an extended filamentary cloud. Here the expansion of the H II region into the ambient molecular cloud leads to the formation of high-mass stars along the dusty filament. In a recent work, based on the spatial and temporal correspondences derived in their analysis, Areal et al. (2020) propose three generations of star formation associated with the massive star LS II +26 8.

In this Letter, we investigate the H II region, G24.47+0.49 (hereafter G24.47), likely ionized by an early O-type star (Garay et al. 1993), to probe possible signatures of hierarchical triggering and multi-epoch star formation. Observed as part of several radio surveys (Wink et al. 1982; Lockman 1989; Churchwell et al. 1990; Garay et al. 1993; Becker et al. 1994; Walsh et al. 1998), G24.47 is associated with IRAS 18314–0720 and is located at a distance of 5.82 kpc (Urquhart et al. 2018). This source is also associated with the massive ($6095\,M_{\odot}$) ATLASGAL clump, AGAL024.471+00.487 (Urquhart et al. 2018). The 4.5, 5.8, and 8.0 μm color-composite Spitzer-IRAC[25] image illustrated in Figure 1(a) presents an interesting morphology, where G24.27 is revealed as a bright ring located at the center of a complex region displaying bubble-like structures, pillars, and arcs.

The Letter is organized as follows. Section 2 discusses the Atacama Large Millimeter/submillimeter Array (ALMA) observations carried out as part of the ALMA Three-millimeter Observations of Massive Star-forming Regions (ATOMS) survey and the other multiwavelength archival data used in this study. Results obtained from the dust continuum, ionized emission, and molecular line analysis are presented in Section 3. Discussion on the three observed epochs of star formation is presented in Section 4, and the overall picture of hierarchical triggering and multi-epoch star formation in G24.47 is discussed in Section 5. Section 6 summarizes the results.

2. Observations and Archival Data

For this study, we have utilized data from the ATOMS survey and other archival data sets. Brief descriptions of these are given in the following subsections.

2.1. ALMA Observations

G24.47 was observed as part of the ATOMS survey (Project ID: 2019.1.00685.S; PI: Tie Liu), which aims to study 146 massive star-forming clumps. Details of the survey can be found in Liu et al. (2020). The 12 m + 7 m combined data for continuum and line emission are used here. The maps have a field of view of 80″ or 2.26 pc at the distance of G24.47 and a maximum recoverable scale of 76.″2 or 2.15 pc. To probe the kinematics and dynamics of the associated ionized and dense gas, we use the H40α hydrogen radio recombination line (RRL) along with $H^{13}CO^{+}$ (1–0) and HCO^{+} (1–0) molecular line transitions. The synthesized beam size for the continuum and H40α is $2.''1 \times 1.''8$. For molecular line observations, they are $2.''4 \times 2.''1$ and $2.''3 \times 2.''0$ for $H^{13}CO^{+}$ and HCO^{+}, respectively. The rms noise is ∼0.65 mJy beam^{-1} for the continuum and ∼[3.5, 8.5, 12] mJy beam^{-1} for the [H40α, $H^{13}CO^{+}$, HCO^{+}] lines at the native velocity resolution of [1.5, 0.2, 0.1] km s^{-1}.

2.2. Archival Data

To probe the radio continuum emission associated with this region, we use Very Large Array (VLA) archival data at 4.86 GHz. The observations were conducted on 1988 March 3 using the VLA C configuration[26] (Legacy ID: AB414; PI: R. Becker). The image is retrieved from the National Radio Astronomy Observatory VLA Archive Survey[27] (NVAS), which has a beam size of $5.''9 \times 3.''9$ and an rms noise of 0.4 mJy beam^{-1}. To identify the ionizing source associated with the H II region, G24.47, we use the near-infrared (NIR) *JHK* photometric data for point sources from the Two Micron All Sky Survey (2MASS; Skrutskie et al. 2006) and UKIRT Infrared Deep Sky Survey (UKIDSS; Lawrence et al. 2007), which were taken during the UKIDSS Galactic Plane Survey Data Release 6 (Lucas et al. 2008). The angular resolution of 2MASS and UKIDSS data are ∼2″ and 0.″9, respectively.

3. Results

3.1. 4.86 GHz and 3 mm Continuum Emission

VLA 4.86 GHz and ATOMS 3 mm continuum maps are shown in Figure 1. The VLA map displays a distinct ring morphology (radius ∼0.8 pc) of bright, ionized gas emission with prominent peaks, a low-emission inner region displaying an almost empty, cavity-like structure at the center, and extended faint emission beyond the ring. Such ringlike morphology of H II regions could be associated with flat, sheetlike parental cloud structures (Beaumont & Williams 2010; Kabanovic et al. 2022). The inner rim of the ring is observed to be dominated by 8.0 μm emission (see Figure 1(a)). This could be attributed to thermal dust emission from the forming hot massive stars in the ring or emission from polycyclic aromatic hydrocarbons (e.g., Watson et al. 2008), which are indicative of photodissociation regions. The ATOMS 3 mm continuum and H40α line emission are also seen to closely trace the bright ring structure (see Figures 1(b) and (c)).

Both the 4.86 GHz and 3 mm maps reveal the presence of compact cores in the bright ring. To understand the nature of these cores, we implement the approach followed by Saha et al. (2022) and use a combination of the `DENDROGRAM` algorithm and the `CASA` *imfit* task to extract the cores. In total, six radio (R1–R6) and ten 3 mm (MM1–MM10) cores are identified.

[25] Images taken from the archives of the Galactic Legacy Infrared Midplane Survey Extraordinaire (Benjamin et al. 2003).

[26] https://science.nrao.edu/facilities/vla/docs/manuals/propvla/array_configs

[27] The NVAS can be browsed through http://www.vla.nrao.edu/astro/nvas/.

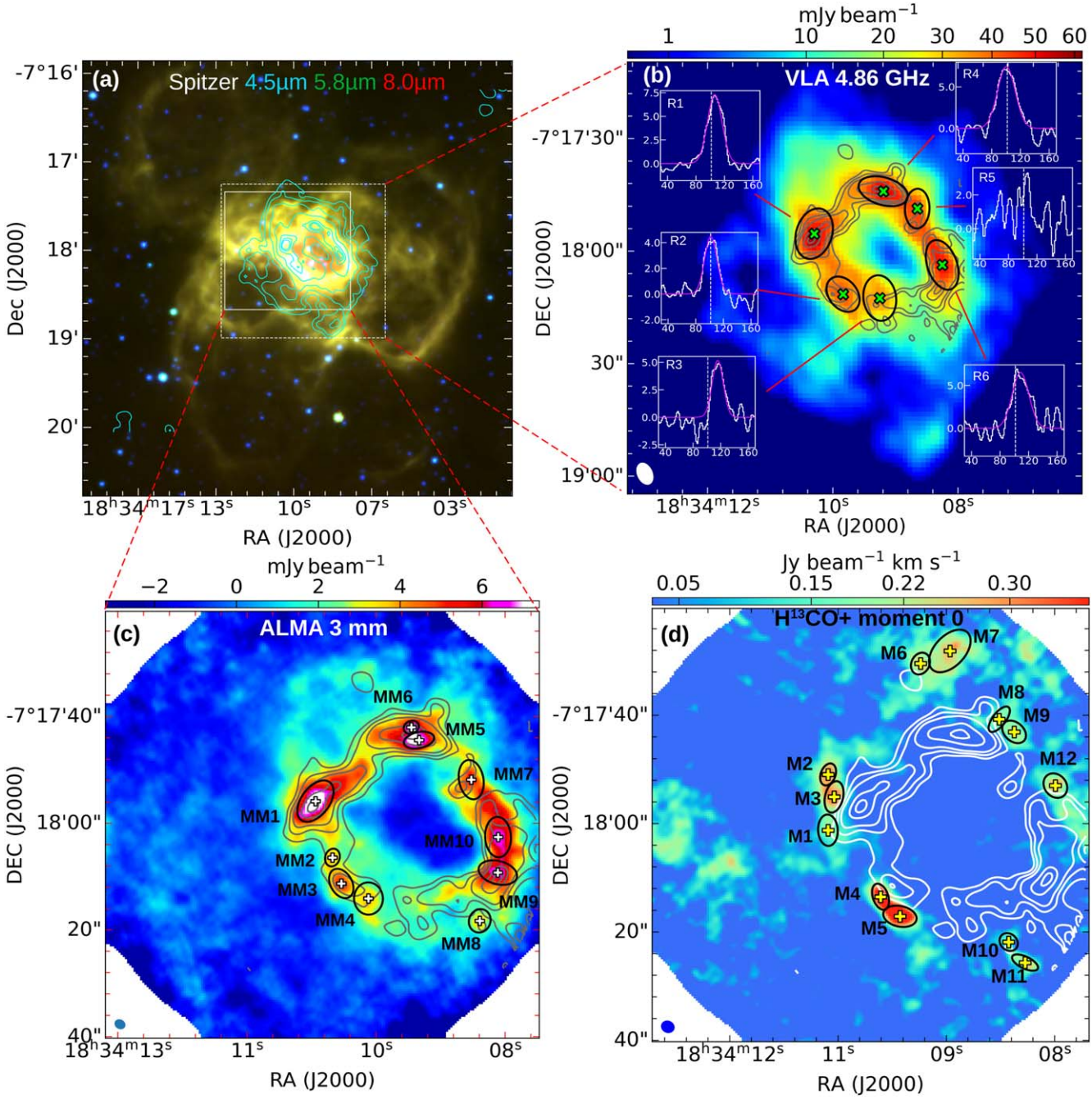

Figure 1. Morphology of the region associated with G24.47. (a) Spitzer-IRAC color-composite image overlaid with VLA 4.86 GHz contours at [3, 7, 20, 50, 90, 110, 120] × σ (=0.4 mJy beam^{-1}). (b) VLA 4.86 GHz map overlaid with ATOMS H40α contours (Gaussian smoothed over 5 pixels) starting at 2σ (=0.04 Jy beam^{-1} km s^{-1}) in steps of 1σ. The displayed ellipses are identified VLA cores with their central positions (X) marked. The insets show the H40α spectra (boxcar smoothed by four channels; velocity resolution of 6.0 km s^{-1}) of the cores along with their respective Gaussian fits. The LSR velocity of 101.5 km s^{-1} is indicated in each. (c) ALMA 3 mm map overlaid with the H40α contours displayed in (b). The displayed ellipses are identified 3 mm cores with their central positions (+) marked. (d) Moment-zero map (3 pixel smoothed using Gaussian kernel) of $H^{13}CO^{+}$ in the velocity range 93.0 to 113.0 km s^{-1}. The displayed ellipses are identified molecular cores with their central positions (+) marked. Ellipses drawn in the lower left corner of (b), (c), and (d) represent the beams of the respective maps displayed.

The retrieved core apertures and the corresponding peak positions are shown in Figures 1(b) and (c). The details of the procedure followed and parameters used are elaborated in Appendix B.

To characterize the radio cores, we calculate the physical parameters such as the emission measure (EM), number of Lyman-continuum photons emitted per second ($N_{\rm Ly}$), and electron density ($n_{\rm e}$) using Equations (6)–(8) from Schmiedeke et al. (2016). For this, we assume the 4.86 GHz emission to be optically thin and adopt the value of the electron temperature to be 6370 K from Quireza et al. (2006). The estimated parameters are tabulated in Table B1.

Of the ten 3 mm cores identified in our study, only the brighter ones (MM1, MM5, and MM6) were detected by Liu et al. (2021) using higher-resolution 12 m array ATOMS data. A similar issue is also discussed in Sanhueza et al. (2019), where the inclusion of more extended emission from a more compact configuration results in a 20% increase in the number

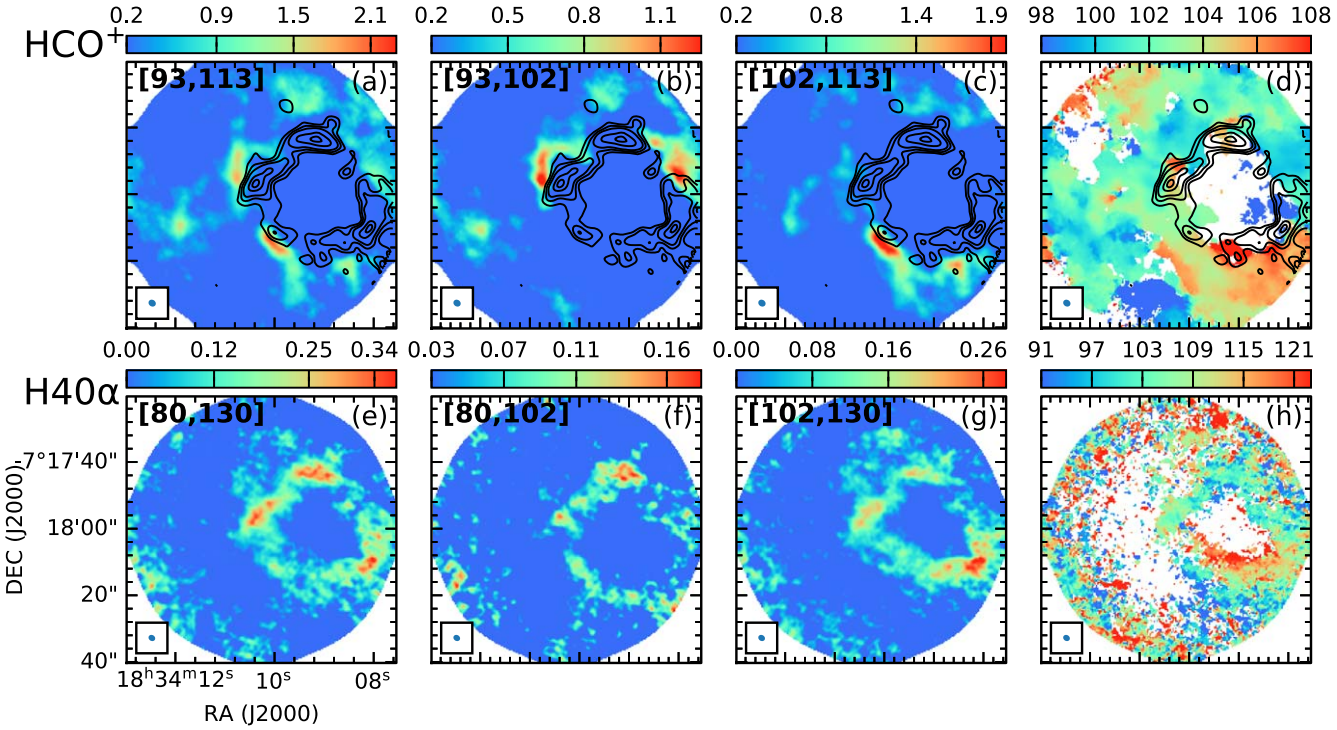

Figure 2. Moment-zero (left three columns) and moment-one (rightmost column) maps of HCO^+ and H40α observed toward G24.47 are shown in panels (a)–(d) and (e)–(h), respectively. The velocity ranges used to obtain the moment-zero maps are given in the top left of each panel. The color bar indicates the flux scale in Jansky per beam kilometer per second and kilometer per second for moment-zero and moment-one maps, respectively. The overlaid contours (in panels (a)–(d)) show the H40α emission (presented as color scale in panel (e)) with contour levels starting at 2σ ($\sigma = 0.04$ Jy beam^{-1} km s^{-1}) in steps of 1σ. These contours are smoothed over 5 pixels using Gaussian kernel. The moment-zero maps (in panels (e)–(g)) are smoothed across 3 pixels using Gaussian kernel. The beam is indicated at the bottom left corner in each panel.

of cores detected. None of these cores show any emission in the molecular line transitions of $H^{13}CO^+$ and HCO^+. This can be inferred from Figures 1(c)–(d), where the 3 mm ring is seen to be mostly devoid of $H^{13}CO^+$ emission, and also, similar distribution is seen for HCO^+ emission (see Figure 2(a)). This suggests that the 3 mm continuum emission is predominantly free–free emission (Keto et al. 2008; Zhang et al. 2023a) with appreciably less contribution from cold dust emission. We verify this by following the method described in Liu et al. (2023) and find six of the 3 mm cores to have more than 50% contribution from free–free emission. However, the existence of hot dust associated with these cores is evident from the presence of mid-infrared (MIR) emission shown in Figure 1(a). Table B2 lists the estimated core parameters.

3.2. Molecular Line Emission

Figure 2(a) shows the distribution of HCO^+ molecular line emission. The molecular line emission encircles the H40α and 3 mm ring. Henceforth, we refer to this as the molecular gas ring, the morphology of which is similar to the ionized gas ring as traced by radio the 4.86 GHz emission. The molecular ring also shows the presence of bright, compact cores. Considering the $H^{13}CO^+$ (1–0) line to be optically thin (e.g., Sanhueza et al. 2012; Saha et al. 2022), we utilize the velocity-integrated intensity (i.e., moment-zero) map of this transition to extract the dense molecular cores. The same procedure as used for extraction of the radio and 3 mm cores is implemented (see Appendix B for details), and ten molecular cores are identified. A careful visual inspection shows the presence of two additional cores that were not detected from this map. For these, we retrieve the parameters using the same approach on the column-density map (see Appendix C). The cores are labeled M1–M12, of which M1 and M10 are extracted from the column-density map. The retrieved apertures are drawn in Figures 1(d) and B1. Core masses are calculated from the generated hydrogen column-density map using

$$M = \mu_{H_2} m_H A \sum N(H_2), \quad (1)$$

where μ_{H_2} and m_H are the mean molecular weight and mass of the hydrogen atom, respectively; A is the pixel area; and $\sum N(H_2)$ is the sum of the column-density values for the pixels in the core area.

Next, to examine the gravitational stability of the cores, we estimate the virial parameter (α_{vir}), which represents the ratio of the virial mass (M_{vir}) to the mass of the individual cores (M_{core}^{mol}). M_{vir} is given by Contreras et al. (2016):

$$M_{vir} = \frac{5\, R_{eff}^{mol}\, \Delta V^2}{8\, \ln(2)\, a_1\, a_2\, G} \sim 209\, \frac{1}{a_1\, a_2} \left(\frac{\Delta V}{\text{km s}^{-1}}\right)^2 \left(\frac{r}{\text{pc}}\right) M_\odot, \quad (2)$$

where R_{eff}^{mol} is the effective radius of the core and ΔV is the line width of the fitted Gaussian profiles to the observed $H^{13}CO^+$ spectra. In the presence of two velocity components, we calculated the average of the line widths obtained from fitting each component individually, following the approach used in Saha et al. (2022). The constant a_1 accounts for the correction for power-law density distribution. It is given as $a_1 = (1 - p/3)/(1 - 2p/5)$

for $p < 2.5$ (Bertoldi & McKee 1992), where we adopt $p = 1.8$ (Contreras et al. 2016). The constant $a_2 = (\arcsin e)/e$ takes into account the shape of the core, e being the eccentricity. The estimated parameters of the molecular cores are listed in Table B3.

3.3. Velocity Structure of G24.47

To inspect and compare the spatial distribution of molecular and ionized gas emission, we created separate moment-zero maps of HCO^+ and H40α over three velocity extents, (i) full velocity range, (ii) blueshifted velocity range (<102 km s^{-1} to 80 or 93 km s^{-1}), and (iii) redshifted velocity range (>102 km s^{-1} up to 113 or 130 km s^{-1}). The moment-zero maps are shown in Figures 2(a)–(c) and (e)–(g). The above velocity ranges are estimated from the average spectra plotted of these line transitions presented in Figure 3(a). The $H^{13}CO^+$ and HCO^+ line profiles show prominent peaks around 101.0 and 104.5 km s^{-1}. On the other hand, the RRL shows a broader profile with a distinct peak at approximately 110.0 km s^{-1}. The systemic velocity of G24.47 is 101.5 km s^{-1} (Schlingman et al. 2011; Urquhart et al. 2018).

As seen from the HCO^+ moment-zero maps, in the velocity range [93, 102] km s^{-1}, the northern part of the molecular gas ring is visible, whereas in the 102 to 113 km s^{-1} range, the emission traces the southern part of the ring. Channel maps (in 1 km s^{-1} bins) are also presented in Appendix A, illustrating the above morphology. Similar morphology is also evident from the $H^{13}CO^+$ transition, where the diffuse emission is less pronounced. Figure 2(d) presents the intensity-weighted mean velocity (i.e., moment-one) map that conforms with the above velocity structure. The northern portion of the molecular ring is blueshifted, and the southern part is redshifted, suggesting expansion of the molecular gas ring. In comparison, the complete ring morphology can be discerned over the entire velocity range for the H40α emission, though the moment-one map (Figure 2(h)) reveals a distinct velocity gradient, similar to that seen in HCO^+.

To examine the velocity field in more detail, we construct a position–velocity (PV) diagram of HCO^+ toward G24.47 along the east–west direction (offset increases from the east to west direction). The PV diagram is shown in Figure 3(b). The integrated intensity map is also included (Figure 3(c)) for easy correlation with the location of the velocity components. Consistent with the moment-one map, the PV diagram also displays signatures of expansion. Velocity differences are evident along the PV cut. Additionally, it displays an almost circular velocity pattern, which is in very good agreement with the results of simulations of expanding shells discussed in the literature (e.g., Arce et al. 2011; Wang et al. 2016). The PV diagram along the north–south direction (not presented here) also shows evidence of expansion but not as prominently. Following the approach outlined in Arce et al. (2011), we obtain a rough estimate of the expansion velocity to be $\sim$9 km s^{-1} by considering the maximum red- and blueshifted velocities observed. This is consistent with the velocity shifts seen in the moment-one map (see Figure 2(d)). Given the lower velocity resolution and signal-to-noise ratio of the H40α emission, it was not possible to evaluate the expansion, if any, of the ionized ring.

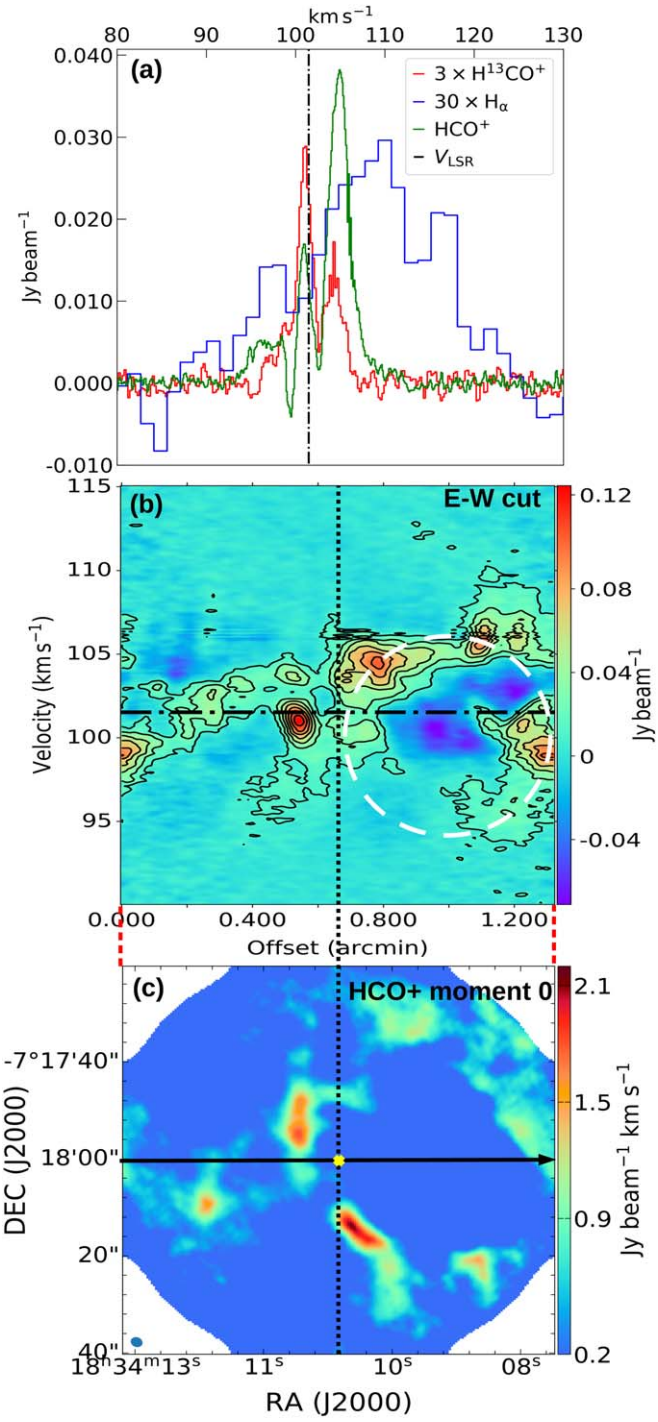

Figure 3. (a) Spectra (averaged over entire molecular ring) of $H^{13}CO^+$ (1–0), HCO^+ (1–0), and H40α toward G24.47 are shown in red, green, and blue lines, respectively. $H^{13}CO^+$ (1–0) and H40α spectra are scaled up by factors of 3 and 30, respectively. H40α spectrum is boxcar smoothed by four channels, resulting in a velocity resolution of 6.0 km s^{-1}. (b) PV diagram of HCO^+ along the PV cut in east–west direction, centered on the ALMA phase center (marked in panel (c)). The contours start at 3σ ($\sigma = 3.0$ mJy beam^{-1}) in steps of 6σ. The circular velocity structure is indicated by the white dashed line. The black dashed–dotted line marks the LSR velocity of 101.5 km s^{-1} in panels (a) and (b). (c) Moment-zero map of HCO^+; this panel is same as Figure 2(a).

4. Discussion

In this section, we probe hierarchical triggering and the multi-epoch massive star formation scenario in G24.47.

4.1. H II Region G24.47

In unveiling the multi-epoch star formation in G24.47, the first one is the massive star(s) responsible for the creation of the

H II region. Based on their 1.5 GHz radio flux density, Garay et al. (1993) proposed a massive ionizing star of spectral type O5.5. We note here that these authors have used the far distance in their analysis. We revisit this estimation using the 4.86 GHz VLA map. Integrating within the 3σ contour and subtracting the contribution from the six detected compact radio cores, the flux density is calculated to be ∼0.9 Jy, which translates to a Lyman-continuum photon flux, $N_{\rm Ly}$, of $\sim 3.4 \times 10^{48}\,{\rm s}^{-1}$. Assuming a single star is responsible for the ionization of G24.47, and comparing the calculated $N_{\rm Ly}$ with that of early-type main-sequence stars tabulated in Panagia (1973), we infer the spectral type to be O8.5V–O8V. However, this can only be considered as a lower limit since dust absorption of Lyman-continuum photons is not accounted for here, which can be significant as shown by many studies (e.g., Paron et al. 2011). The central cavity of G24.47, which is observed to be mostly dust free and devoid of molecular line emission, is likely to be carved out by the powerful radiation and wind of the massive star(s). We attempt to identify the ionizing star(s) by studying the stellar population located within the observed ionized gas emission. This is carried out using NIR color–magnitude and color–color plots (e.g., Potdar et al. 2022). For our study, we have used 2MASS and UKIDSS data sets. The detailed procedure is discussed in Appendix D. Following this, 12 candidate massive (with spectral type earlier than B3) class III stars, namely, E1–E12, are identified within the VLA radio emission. The location of these are shown in Figure D1(c). The positions and *JHK* magnitudes of these sources are listed in Table D1.

By a simple argument, the symmetry of the ionized ring morphology suggests a centrally located ionizing star or a group of ionizing stars. The sources, E10, E11, and E12 are located at the center of the cavity. However, their spectral types from the color–magnitude plot lie between ∼B3−B0.5. So the individual or the sum of their Lyman-continuum photon flux is not consistent with that calculated from the observed 4.86 GHz flux density. The other identified early-type stars are mostly located on the bright, ionized ring. These could be bona fide ionizing sources since it is possible that the ionizing star is displaced from the center due to its proper motion. Such a geometry is observed in the Orion Veil bubble, where the exciting massive star, θ^1 Ori C, is seen offset from the center (see Figure 3 of Pabst et al. 2019). Furthermore, simulations of expanding H II regions, discussed in Mac Low et al. (2007) and Hunter et al. (2008), also show the possibility of formation of nearly spherical shells with off-center ionizing source. Under this scenario, sources E2, E3, E4, and E8 are potential candidates. The NIR spectral type inferred from the color–magnitude diagram is reasonably consistent with the estimated radio spectral type. The above analysis, however, restricts any conclusive identification of the ionizing star of G24.47.

4.2. The Inner Ring: Radio and 3 mm Continuum Emission

Six radio cores are identified in this inner ring of ionized gas. Summarizing the results, we find the radius ($R_{\rm core}^{\rm VLA}$), EM, $n_{\rm e}$, and $M_{\rm ion}$ in the ranges of ∼[0.1, 0.2] pc, $[1.6,\ 2.5] \times 10^6\,{\rm cm}^{-6}$ pc, $[2.3,\ 3.0] \times 10^3\,{\rm cm}^{-3}$, and $[0.5,\ 1.2]\,M_\odot$, respectively. In the same order, the median values are estimated to be 0.28 pc, $2.2 \times 10^6\,{\rm cm}^{-6}$ pc, $2.8 \times 10^3\,{\rm cm}^{-3}$, and $0.8\,M_\odot$. The derived radio properties of these compact VLA cores are consistent with those of UCH II/compact H II regions (Kurtz 2005; Martín-Hernández et al. 2005; de la Fuente et al. 2020; Yang et al. 2019; Yang et al. 2021; Patel et al 2023). It is to be noted that the presence of extended, diffuse emission could possibly result in large extracted core sizes, leading to underestimation of $n_{\rm e}$ and EM. Except for the core R5 (due to poor signal-to-noise ratio), the H40α spectra of the other cores are fitted with a single Gaussian profile (see Figure 1(b)). The line widths are estimated to be in the range ∼[19, 29] km s^{-1}, typical of UCH II/compact H II (Hoare et al. 2007; Liu et al. 2021; Yang et al. 2021).

The inference of the VLA cores representing the intermediate phase between an evolved UCH II region and an early compact H II region is further supported by the identification of radio counterparts from the CORNISH survey.[28] Based on the derived radio properties and association with NIR and MIR emissions, the classification of the sample of CORNISH UCH II regions is robust and reliable (Kalcheva et al. 2018). VLA cores, R1, R4, and R5, are classified as UCH II regions, G024.4721+00.4877, G024.4736+00.4950, and G024.4698 +00.4954 (Kalcheva et al. 2018). Core R3 is also detected in the CORNISH survey but not classified as it does not meet the criteria of flux density greater than 7σ.

From the ATOMS 3 mm continuum map, we identify ten cores. The estimated radii lie in the range $\sim[3.7, 9.6] \times 10^{-2}$ pc with a median value of 7.4×10^{-2} pc. The cores, MM1, MM5, and MM10, are cospatial with radio cores R1, R4, and R6, respectively. Radio core R4 is likely fragmented to MM5 and MM6 in the higher-resolution ATOMS continuum map. The ATOMS cores, MM3, MM4, and MM9, which do not have radio counterparts, display single-component Gaussian H40α line profiles. The fitted line widths are in the range ∼[19, 32] km s^{-1}. Given the absence of *cm* emission, these could be conjectured as very early stages of massive stars in the HC/UC H II region phase (Liu et al. 2021). The H40α spectra for cores MM2, MM7, and MM8 have poor signal-to-noise, and hence, it is difficult to probe their nature.

With the detection of the ring of bright radio and 3 mm continuum emission harboring HC, UC, and compact H II regions, we are likely witnessing a burst of the second epoch of massive star formation. The location of these regions broadly aligns with the theoretical predictions of Mac Low et al. (2007). Here, the authors simulate the dynamical expansion of a H II region into turbulent, self-gravitating gas driven by the ionized gas's overpressure, sweeping up a shell of gas. Theoretically, this shell expands in $\sim 10^5$ yr to a radius of ∼1 pc, and subsequently, the ionized gas breaks out of the natal cloud. The results of this simulation show that an episode of secondary collapse ensues in the shell, where existing turbulent density fluctuations in the shell lead to collapse of self-gravitating cores. Consistent with these predictions, Hunter et al. (2008) present a case study of the UCH II region G5.89-0.39, where they identified multiple 875 μm cores confined to the expanding shell formed in the process of secondary collapse.

The simulations of Mac Low et al. (2007), however, showed the formation of externally ionized, low-mass, transient cores in the shell, masquerading as UCH II regions. In our case, 75% of the VLA and ATOMS cores are inferred to be in the early phases of HC, UC, or compact H II regions. From the estimated Lyman-continuum photon flux, the compact H II regions are likely ionized by zero-age main-sequence (ZAMS) stars with spectral type B0−O8.5 (Panagia 1973; see Table B1). Even though the $H-K$ uncertainty allows for the source E4 to be

[28] Coordinated Radio "*N*" Infrared Survey for High-mass Star Formation (CORNISH; Purcell et al. 2013).

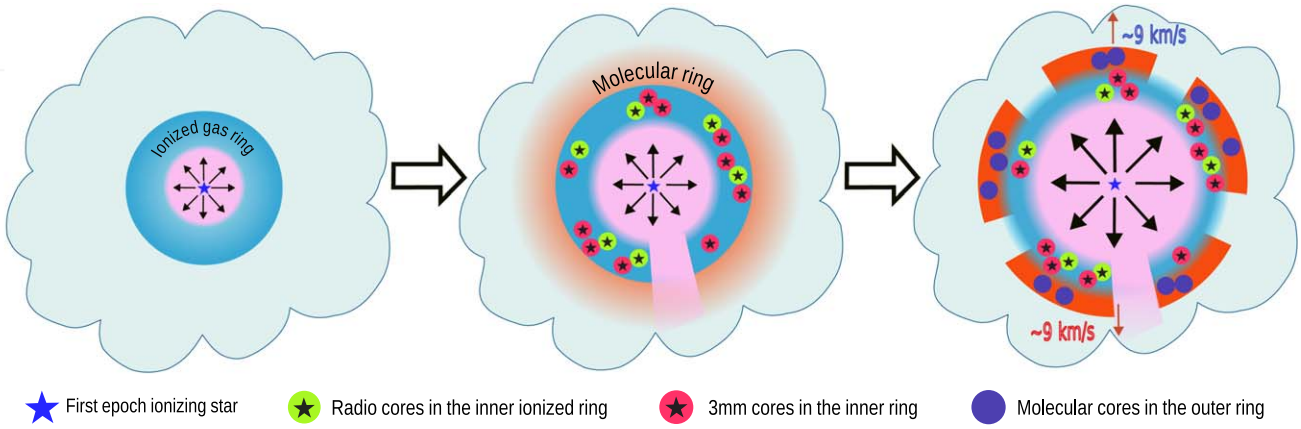

Figure 4. A schematic of the hierarchical triggering of multi-epoch massive star formation in G24.47.

considered as a class III source, in all likelihood it is a class II young stellar object (Figure D1(b)), and located within ∼3″, it is possibly the ionizing source of the compact H II region, R1.

4.3. Expanding Molecular Ring

A molecular ring is clearly visible from the moment-zero maps of $H^{13}CO^+$ (1–0) (see Figure 1(d)), HCO+ (see Figures 3(a)–(c)), and the column-density map (see Figure B1). The expansion of this ring is evident from the investigation of the gas kinematics in Section 3.3.

Twelve molecular cores are identified in this molecular gas ring. The radius, mass, surface mass density, and the virial parameter of the cores lie in the range [0.05, 0.1] pc, [4.3, 30.1] $M_\odot$, [0.1, 0.4] g cm^{-2}, and [0.7, 3.8], respectively. In the same order, the median values are estimated to be 0.06 pc, 8.8 $M_\odot$, 0.2 g cm^{-2}, and 1.8. For all the detected molecular cores, the estimated surface mass densities satisfy the threshold of 0.05 g cm^{-2} proposed by Urquhart et al. (2014) for massive star formation. It is worth noting here that in the recent Querying Underlying Mechanisms of Massive Star Formation with ALMA-resolved Gas Kinematics and Structures (QUARKS) survey (Liu et al. 2024), nearly half of the identified cores have dense 1.4 mm cold dust counterparts, thus confirming their tendency to form stars. Gauging their gravitational stability, we find that 50% of the cores have $\alpha_{\rm vir} < 2$, indicating that these are supercritical and under gravitational collapse in the absence of other supporting mechanisms, such as magnetic fields (Kauffmann et al. 2013; Tang et al. 2019). The other 50% are subcritical cores with $\alpha_{\rm vir} > 2$. These are gravitationally unbound and represent transient objects unless one considers other mechanisms, such as magnetic field or external pressure, that would confine these structures (Kauffmann et al. 2013; Li et al. 2020). In the case of G24.47, feedback from the newly formed massive stars in the ionized ring and the evidence of the expansion suggest that external pressure will play a key role in confining these compact cores. We searched for infall signature using the $H^{13}CO^+$ (1–0) and HCO^+ spectra extracted toward these cores but did not find any conclusive evidence. This could be attributed to the possibility that infall signatures are blended with complex dynamics in the molecular ring, including expanding motions and feedback from stellar winds. Further, in the interferometric observations, we may be missing the total power, which makes it difficult to identify absorption features.

Supporting the active star formation activity, we have identified one 70μm point source within ∼2.″5 of M12 from the Herschel PACS point source catalog (Herschel Point Source Catalogue Working Group et al. 2020). This finding serves as compelling evidence for the presence of an embedded protostar, as external heating cannot raise temperatures high enough to emit at this wavelength (Stutz et al. 2013).

5. Hierarchical Triggering of Multi-epoch Massive Star Formation

Based on our detailed analysis, we propose an interesting picture of multi-epoch massive star formation observed in the G24.47 complex. Our hypothesis is illustrated in the schematic presented in Figure 4. The observed hierarchy is initiated with the birth of a massive star in a self-gravitating natal cloud forming a H II region. The thermal overpressure of the warm ionized gas then drives the expansion of the H II region. This leads to a swept-up ring where secondary collapse occurs, thus triggering the second epoch of star formation. In G24.47, we detect a very active high-mass star formation episode in this inner ionized ring with a host of newly formed stars in the early to intermediate evolutionary phases of HC, UC, and compact H II regions with detected RRL and cm emission.

To support the above inference, we estimate the dynamical timescale of the expanding H II region and compare the same with the typical ages of the HC, UC, and compact II regions, following the discussion outlined in Liu et al. (2016) and Das et al. (2017). For a H II region expanding into a homogeneous medium, the dynamical age is given by Dyson & Williams (1980):

$$t_{\rm dyn} = \frac{4}{7}\frac{R_{\rm St}}{C_{\rm H\,II}}\left[\left(\frac{R_{\rm IF}}{R_{\rm St}}\right)^{7/4} - 1\right], \quad (3)$$

where

$$R_{\rm St} = (3N_{\rm Ly}/4\pi n_0^2 \alpha_{\rm B})^{1/3}. \quad (4)$$

In the above equations, $C_{\rm H\,II}$ is the isothermal sound speed (assumed to be 10 km s^{-1}), $R_{\rm IF}$ is the radius of the ionized ring (∼0.8 pc), $\alpha_{\rm B}$ is the radiative recombination coefficient taken as $2.6 \times 10^{-13}(10^4\,{\rm K/T})^{0.7}$ cm^3 s^{-1} (Kwan 1997), and n_0 is the initial particle density of the ambient gas. We estimate $n_0 \sim 10^4$ cm^{-3} from the retrieved ATLASGAL map (see Appendix E), with the

assumption that the physical properties, like density, do not change over evolutionary stages (from quiescent to H II regions) in the star formation process (Urquhart et al. 2022). Thus, the dynamical age of the H II region is calculated to be $\sim 2 \times 10^5$ yr. This ensures sufficient time for the formation of the identified UC and compact H II regions in the inner ionized ring, given the typical lifetimes of these to be $\sim 10^4$–10^5 yr (Churchwell 2002; Davies et al. 2011).

In recent studies, evidence of expanding ionized ([C II]) shells has been found in windblown bubbles (e.g., Orion Veil; Pabst et al. 2019, RCW 120; Luisi et al. 2021, NGC 628; Mayya et al. 2023). Indication of such an expansion of the inner ionized ring in G24.47 is seen from the velocity structure probed with the H40α RRL emission. However, the picture that emerges from the investigation of the molecular gas kinematics reveals, perhaps for the first time, a direct and unambiguous signature of an expanding molecular ring in G24.47.

The total mass of the molecular ring ($M_{\rm shell}$) is estimated to be $\sim 515\,M_\odot$ from the column-density map. Taking the expansion velocity ($v_{\rm exp}$) of $\sim 9\,{\rm km\,s^{-1}}$, the kinetic energy ($0.5 M_{\rm shell} v_{\rm exp}^2$) of the expanding ring is calculated to be $\sim 4 \times 10^{47}$ erg. Addressing the energy feedback from the H II region, we estimate the kinetic and thermal energies of the ionized gas to be $\sim 6 \times 10^{46}$ erg and $\sim 3 \times 10^{46}$ erg, respectively, using the expressions from Xu et al. (2018) and Li et al. (2022). Individually, these are an order of magnitude lower than the kinetic energy of the molecular shell. Our results are similar to those seen in RCW 120 (Luisi et al. 2021) and Orion Veil (Pabst et al. 2019), where the authors attribute this to leakage of hot plasma into the surroundings. Indeed, the radio ring in G24.47 is observed to be broken toward the southwest (see Figure 1), which was also reported by Garay et al. (1993).

Theoretical studies (e.g., Haid et al. 2018) predict that the energy injection from ionized gas into the surrounding medium would dominate that of the stellar wind. To confront the energetics with the creation of the expanding molecular ring in G24.47, we further probe the efficiency of the wind power. Considering a single ionizing O8.5V–O8V star for G24.47, as inferred from the radio flux density, we determine the wind luminosity ($3.2 \times 10^{35} \dot{M} v_{\rm w}^2$; $\dot{M}$ being the mass-loss rate in solar mass per year and $v_{\rm w}$ the wind velocity in kilometer per second). Using the parameter values for these spectral types from Martins & Palacios (2017), we estimate the wind luminosity to be $(4$–$5) \times 10^{34}\,{\rm erg\,s^{-1}}$. This translates to mechanical energy $\sim 3 \times 10^{47}$ erg injected by wind of the ionizing star over the dynamical age of the H II region. This is comparable to the kinetic energy of the molecular gas ring, thus indicating efficient conversion of the mechanical energy of the wind to kinetic energy of the ring driving its expansion. Note that in the above analysis, we have not considered the inclination angle, if any, of the molecular gas ring and the winds from newly formed stars in the ionized ring.

Summarizing the analysis of the energetics, we infer that the total energy budget from the ionizing radiation (both kinetic and thermal) and the stellar wind is sufficient for the creation and expansion of the molecular ring, with the wind kinetic power being possibly the most efficient player.

Furthermore, SO emission, a tracer of low-velocity shocks from H II regions (Liu et al. 2020), is seen (not presented here) to be cospatial with the observed $H^{13}CO^+$ (1–0) and HCO^+ (1–0) molecular ring. Coupled with the feedback from the newly formed massive stars, a third epoch of triggered massive star formation is observed in this expanding molecular ring, where potential high-mass star-forming molecular cores are identified. A scenario of "collect and collapse" (CC) is evident, where gravitational instabilities result in the fragmentation of the swept-up ring to molecular condensations that further fragment into the cores that are observed. Consistent with the prediction of the CC hypothesis (Deharveng et al. 2003), these condensations, in the form of core clusters (i.e., M1–M3, M4–M5, M6–M7, M8–M9, M12, and M10–M11 apparently corresponding to six core clusters; see Figure 1(d)), are observed to be almost *regularly* spaced in the molecular gas ring enveloping the inner ionized ring.

6. Conclusions

Evidence for triggered star formation linking several epochs of stars around H II regions is difficult to assemble. It is challenging to associate evolved massive stars with the next epoch of star-forming regions, each of which must show indications of ongoing star formation activity. Based on a detailed continuum and multispectral line study of G24.47 using data from the ATOMS survey and archival radio and infrared data, we provide evidence of hierarchical triggering of three epochs of massive star formation. The first is the massive star(s) responsible for forming the H II region G24.47. Using the 4.86 GHz VLA map, we propose the spectral type to be O8.5V–O8V. The inner ring of enhanced radio and 3 mm emission comprises the next epoch of massive stars, which formed due to secondary collapse of the swept-up material. We detected six radio and ten 3 mm cores showing signatures of various evolutionary phases, ranging from the initial stages of gravitational collapse to intermediate phases between UC and compact H II regions. The molecular gas kinematics analysis unveils direct evidence of an expanding molecular ring powered by the ionized radiation and the stellar wind kinetic energy. Furthermore, the molecular gas ring expanding at $\sim 9\,{\rm km\,s^{-1}}$ hosts the third epoch of potential massive star-forming regions, where we identified twelve molecular cores. Virial analysis indicates that 50% of them are supercritical and in gravitational collapse. This observational evidence strongly advocates for more detailed case studies to address the exact influence of expanding H II regions in triggering further star formation. Detailed kinematic studies of the ionized and neutral material in a sample of promising candidates, utilizing high-resolution data, are essential to understand the underlying physical processes.

Acknowledgments

The authors thank the referee for insightful comments/suggestions that helped improve the manuscript. This work has been supported by the National Key R&D Program of China (No. 2022YFA1603101). H.-L.L. is supported by National Natural Science Foundation of China (NSFC) through the grant No. 12103045, by Yunnan Fundamental Research Project (grant No. 202301AT070118, 202401AS070121), and by Xingdian Talent Support Plan—Youth Project. T.L. acknowledges the support by the National Key R&D Program of China (No. 2022YFA1603101), National Natural Science Foundation of China (NSFC) through grants Nos. 12073061 and 12122307, the international partnership program of Chinese Academy of

Sciences through grant No. 114231KYSB20200009, and the Tianchi Talent Program of Xinjiang Uygur Autonomous Region. G.G. and L.B. acknowledge support by the ANID BASAL project FB210003. This work was performed in part at the Jet Propulsion Laboratory, California Institute of Technology, under contract with the National Aeronautics and Space Administration (80NM0018D0004). This work is sponsored (in part) by the Chinese Academy of Sciences (CAS), through a grant to the CAS South America Center for Astronomy (CASSACA) in Santiago, Chile. M.J. acknowledges support from the Research Council of Finland grant No. 348342. J.O.C. acknowledges financial support from the South African Department of Science and Innovation's National Research Foundation under the ISARP RADIOMAP Joint Research Scheme (DSI-NRF grant No. 150551). This Letter makes use of the following ALMA data: ADS/JAO. ALMA#2019.1.00685.S. ALMA is a partnership of ESO (representing its member states), NSF (USA), and NINS (Japan), together with NRC (Canada), MOST and ASIAA (Taiwan), and KASI (Republic of Korea), in cooperation with the Republic of Chile. The Joint ALMA Observatory is operated by ESO, AUI/NRAO, and NAOJ. This research made use of astrodendro, a Python package to compute dendrograms of Astronomical data (http://www.dendrograms.org/). This research made use of Astropy, a community-developed core Python package for Astronomy (Astropy Collaboration et al. 2018).

Appendix A
Channel Map

The channel map of HCO^+ is shown in Figure A1.

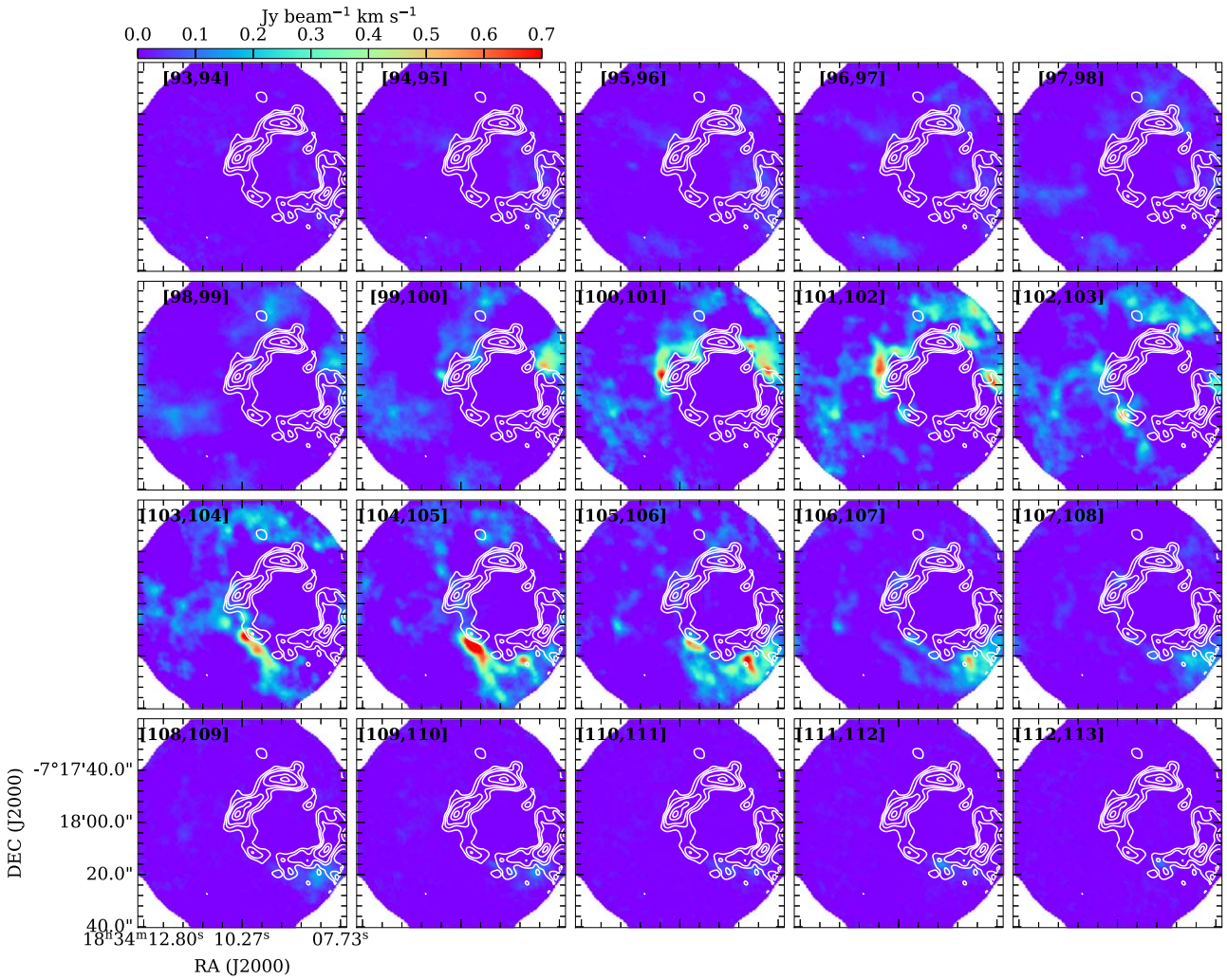

Figure A1. Channel maps of HCO^+ overlaid with H40α contours (Gaussian smoothed over 5 pixels) with levels starting at 2σ ($\sigma = 0.04$ Jy beam^{-1} km s^{-1}) in steps of 1σ. Each panel shows the velocity-integrated intensity within a velocity range of 1 km s^{-1}. The velocity range is mentioned in the top left of each panel.

Appendix B
Core Extraction

Following the approach used in Li et al. (2020), Liu et al. (2021, 2022), and Saha et al. (2022), cores are extracted by utilizing the ASTRODENDRO package and the CASA *imfit* task. Initially, in the DENDROGRAM algorithm (Rosolowsky et al. 2008), for extraction of the radio and 3 mm cores, we set *min_value* $= 3\sigma$ and *min_delta* $= \sigma$, where σ represents the rms noise of the corresponding map. The min_npix parameter is set to be equivalent to the synthesized beam area for extracting the 3 mm cores and half of the synthesized beam area to detect the radio cores. Subsequently, the CASA *imfit* task is employed with the DENDROGRAM parameter estimates as initial guess values. In our study, we only concentrated on the structures located on the ring. To ensure the exclusion of spurious cores, we retain only the cores with peak flux greater than 5σ. Furthermore, we also reject cores with poorly fitted shapes by visual inspection of the map overlaid with the identified structures and discarded structures located at the edge that appeared truncated. This process identified six radio (R1–R6) and ten 3 mm cores (MM1–MM10), which are shown as ellipses in Figures 1(b) and (c), respectively. It should be noted that in the case of 3 mm cores MM5 and MM6, which are also identified in Liu et al. (2021), they are manually fitted using CASA *imfit* since the DENDROGRAM algorithm resolved it into a single leaf though two distinct cores are seen visually. The estimated parameters of the radio and 3 mm cores are listed in Table B1 and Table B2, respectively.

In the case of the molecular cores, we employed the same procedure on the moment-zero map of $H^{13}CO^+$ (see Figure 1(d)) taken over the velocity range of 93.0 to 113.0 km s^{-1}. Ten cores (M2–M9 and M11–M12) are identified. Two additional cores (M1 and M10) are extracted from the column-density map obtained using $H^{13}CO^+$ and HCO^+ (see Appendix C). We only concentrated on the structures on the molecular gas ring encompassing the ionized ring. The spatial distribution of the detected molecular cores overlaid on the moment-zero map of $H^{13}CO^+$ and the column-density map are illustrated in Figures 1(d) and B1, respectively. Table B3 lists the estimated molecular core parameters.

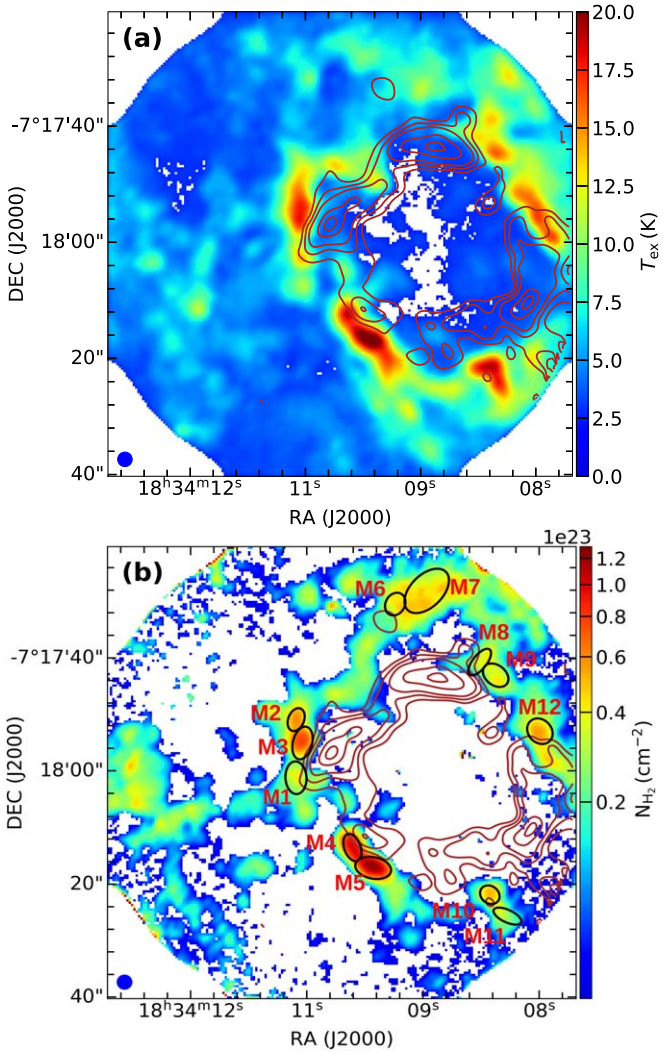

Figure B1. (a) Effective line-of-sight excitation temperature map generated using HCO^+. (b) Column-density map toward G24.47, generated using molecular transitions $H^{13}CO^+$ and HCO^+. The ellipses represent the apertures of identified molecular cores. In both panels, the overlaid contours show the H40α emission with contour levels starting at 2σ ($\sigma = 0.04$ Jy beam^{-1} km s^{-1}) in steps of 1σ. These contours are smoothed over 5 pixels using Gaussian kernel. The beam size of 2.″5 is indicated at the bottom left.

Table B1
Parameters of VLA Cores

Core	Peak Position		Deconvolved Size	$R_{\rm core}^{\rm VLA}$	$F_{\rm int}^{4.86}$	$N_{\rm ly}$	EM	$n_{\rm e}$	$M_{\rm ion}$[a]	$V_{\rm LSR}$[b]	ΔV[b]	Spectral Iype
	R.A. (J2000)	Decl. (J2000)	(arcsec × arcsec)	(pc)	(mJy)	(10^{47} s^{-1})	(10^{6} cm^{-6} pc)	(10^{3} cm^{-3})	($M_{\odot}$)	(km s^{-1})	(km s^{-1})	
R1	18:34:10.33	−7:17:55.38	13.8 × 9.6	0.16	383.5	14.1	2.3	2.7	1.2	106.4	24.3	O9–O8.5
R2	18:34:09.81	−7:18:11.53	10.5 × 7.6	0.13	200.6	7.4	2.0	2.8	0.6	101.8	21.2	O9.5–O9
R3	18:34:09.15	−7:18:12.56	12.2 × 8.8	0.15	207.1	7.6	1.6	2.3	0.7	115.8	18.9	O9.5–O9
R4	18:34:09.08	−7:17:44.06	13.6 × 7.4	0.14	308.9	11.4	2.5	3.0	0.9	100.4	28.6	O9.5–O9
R5	18:34:08.51	−7:18:48.71	10.6 × 6.6	0.12	186.1	6.8	2.2	3.0	0.5	…[b]	…[b]	B0–O9.5
R6	18:34:08.02	−7:18:03.72	13.8 × 7.9	0.15	293.8	10.8	2.2	2.7	0.9	108.8	27.6	O9.5–O9

Notes.

[a] Mass of ionized gas, $M_{\rm ion} = \frac{4}{3}\pi (R_{\rm core}^{\rm VLA})^3 n_{\rm e} m_{\rm p}$.

[b] $V_{\rm LSR}$ and ΔV are obtained from ATOMS H40α transition. For R5, the spectrum is not fitted with Gaussian as it shows a high signal-to-noise ratio (see Figure 1(b)).

Table B2
Parameters of Detected Cores from the ALMA 3 mm Map

Core	Peak Position		Decon. Size	$R_{\rm core}$[a]	$F_{\rm peak}^{\rm 3mm}$	$F_{\rm int}^{\rm 3mm}$	$V_{\rm LSR}$	ΔV[b]
	R.A. (J2000)	Decl. (J2000)	(arcsec × arcsec)	(10^{-2} pc)	(mJy beam^{-1})	(mJy)	(km s^{-1})	(km s^{-1})
MM1	18:34:10.35	−7:17:55.88	8.8 × 5.2	9.6	8.3	111.8	105.7	24.9
MM2	18:34:10.14	−7:18:06.45	3.4 × 2.7	4.0	4.5	15.5	…[c]	…[c]
MM3	18:34:10.03	−7:18:11.31	5.9 × 4.0	6.8	5.2	38.2	98.1	23.6
MM4	18:34:09.69	−7:18:14.13	6.1 × 5.4	8.0	4.0	38.6	98.1	19.4
MM5	18:34:09.07	−7:17:44.44	5.7 × 3.0	5.8	7.6	43.1	101.1	25.7
MM6	18:34:09.16	−7:17:42.02	2.9 × 2.3	3.7	7.6	20.7	99.6	27.3
MM7	18:34:08.42	−7:17:51.85	7.4 × 4.5	8.0	5.3	53.5	…[c]	…[c]
MM8	18:34:08.31	−7:18:18.31	4.5 × 3.9	5.9	3.7	20.9	…[c]	…[c]
MM9	18:34:08.09	−7:18:09.27	7.2 × 4.3	7.9	6.9	64.8	116.0	32.2
MM10	18:34:08.08	−7:18:02.61	7.6 × 4.8	8.5	6.8	73.2	106.5	23.4

Notes.
[a] $R_{\rm core}$ is the core radius taken to be half of the geometric mean of $\rm FWHM_{maj}$ and $\rm FWHM_{min}$ at the core distance.
[b] ΔV is derived from ATOMS H40α transition.
[c] Spectra of MM2, MM7, and MM8 have poor signal-to-noise ratio.

Table B3
Parameters of Molecular Cores

Core	Peak Position		Decon. Size	$R_{\rm eff}^{\rm mol}$[a]	ΔV	$N(\rm H_2)$[b]	$n_{\rm H_2}$[c]	$M_{\rm core}^{\rm mol}$	Σ[d]	$M_{\rm vir}$	$\alpha_{\rm vir}$
	R.A. (J2000)	Decl. (J2000)	(arcsec × arcsec)	(10^{-2} pc)	(km s^{-1})	(10^{22}cm^{-2})	(10^{5}cm^{-2})	($M_\odot$)	(g cm^{-2})	($M_\odot$)	
M1	18:34:10.79	−07:18:01.24	5.8 × 3.7	6.5	1.2	3.1	1.2	9.2	0.1	14.4	1.4
M2	18:34:10.79	−07:17:50.95	4.3 × 2.7	4.7	1.3	5.3	2.6	8.3	0.2	12.4	1.3
M3	18:34:10.71	−07:17:55.09	5.9 × 3.3	6.2	1.2	5.8	2.2	15.7	0.3	12.5	0.7
M4	18:34:10.14	−07:18:13.52	5.0 × 2.8	5.3	2.5	8.4	3.9	16.2	0.4	48.2	2.5
M5	18:34:09.90	−07:18:16.81	6.2 × 3.8	6.9	1.5	8.8	3.1	28.6	0.4	22.5	0.7
M6	18:34:09.65	−07:17:30.47	4.2 × 3.3	5.3	2.0	4.1	1.8	7.7	0.2	32.4	3.8
M7	18:34:09.29	−07:17:28.14	9.4 × 5.6	10.2	2.5	4.2	1.0	30.1	0.2	93.8	2.7
M8	18:34:08.68	−07:17:40.75	5.6 × 2.5	5.2	1.2	3.1	1.5	6.1	0.2	10.6	1.4
M9	18:34:08.50	−07:17:43.08	4.9 × 3.5	5.8	1.3	3.5	1.5	8.4	0.2	14.2	1.5
M10	18:34:08.56	−07:18:21.89	5.5 × 3.3	6.0	1.6	4.3	1.0	6.3	0.1	22.2	3.0
M11	18:34:08.36	−07:18:25.68	5.2 × 2.2	4.8	1.3	2.6	1.3	4.3	0.1	11.7	2.1
M12	18:34:07.99	−07:17:53.00	4.8 × 4.0	6.2	2.1	4.6	1.8	12.5	0.2	38.5	2.9

Notes.
[a] $R_{\rm eff}^{\rm mol}$ is the effective radius of core equaling half of the geometric mean of major and minor axes at the source distance.
[b] Mean value of $N(\rm H_2)$.
[c] Number density ($n_{\rm H_2} = 3M_{\rm core}^{\rm mol}/4\pi(R_{\rm eff}^{\rm mol})^3\mu_{\rm H_2}m_{\rm H}$).
[d] Mass surface density ($\Sigma = M_{\rm core}/\pi(R_{\rm eff}^{\rm mol^d})^2$).

Appendix C
Column Density

Following the method discussed in Xu et al. (2023), we generate the column-density map. First, we assumed $\rm HCO^+$ to be optically thick (optical depth, $\tau \gg 1$) and determined the effective line-of-sight excitation temperature ($T_{\rm ex}$) for each pixel in the $\rm HCO^+$ spectral cube, following the discussion given in Appendix F of Xu et al. (2023). For our analysis, we considered only the pixels where the peak intensity along the

spectral axis is greater than 4 times rms. We convolved the data cubes of HCO^+ and $H^{13}CO^+$ to a common beam size of 2.″5 and also assumed that the two molecules share the same T_{ex}. Further considering the excitation temperature to be equal to the kinetic temperature for all the energy states and the levels populated according to Boltzmann distribution, the $H^{13}CO^+$ column density at each pixel is calculated using Equation (11) of Xu et al. (2023). Furthermore, we have adopted an abundance ratio of $H^{13}CO^+$ to H_2 of 1.28×10^{-10}, as determined by Hoq et al. (2013) in their investigation of 333 high-mass star-forming regions using MALT90 data. The generated excitation temperature and hydrogen column-density maps are presented in Figures B1(a) and (b), respectively.

Appendix D
Ionizing Massive Star(s)

To search for candidate ionizing star(s), we select a region covering the observed radio emission. The NIR color–magnitude and color–color plots for the selected region are shown in Figures D1(a) and (b). UKIDSS data has saturation limits of 12.65, 12.5, and 12 mag in *J*, *H*, and *K*, respectively (Lucas et al. 2008). Hence, for sources brighter than this, 2MASS data are used. To ensure that the retrieved sample are sources with good-quality photometry, we include 2MASS sources with "read-flag" = 2 and UKIDSS sources with "pstar" > 0.94 and "cl" = −1. To account for the zero-point photometric offset between the two data sets used, we adopt the approach used by, e.g., Saral et al. (2017). For this, we consider a large (radius of 2.′5) region centered on G24.47 and estimate the median and standard deviation of the photometric offset between UKIDSS and 2MASS for sources detected in both data sets. Median values of 0.09, −0.06, and −0.03 are calculated for *J*, *H*, and *K* bands, respectively, with a standard deviation of 0.1 in each band. Subsequently, we apply an offset of 0.09 ± 0.1, -0.06 ± 0.1, and -0.03 ± 0.1 mag, respectively, to the *J*, *H*, and *K* magnitudes of UKIDSS.

From the color–magnitude diagram, we identify 23 massive stars earlier than the B3 spectral type. Next, we compare their location with that of class III sources. Taking the photometric and offset uncertainties into account, of the 23 identified stars, 12 lie within the reddening vectors of B3 and O5. These are labeled E1–E12, and the locations of these are shown in Figure D1(c), and the details of these sources are listed in Table D1.

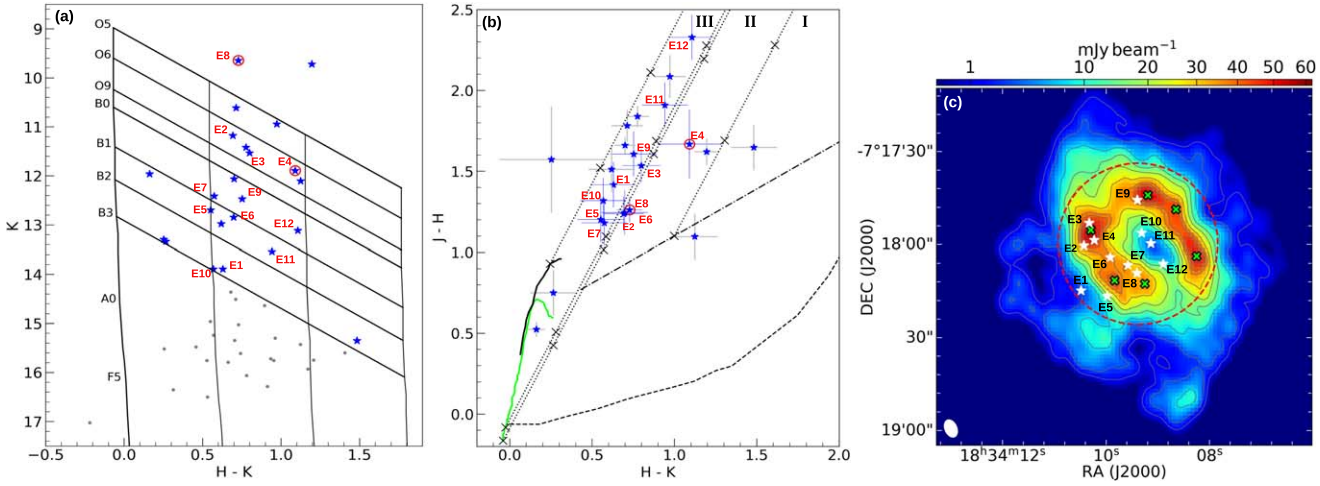

Figure D1. (a) The color–magnitude diagram of the sources associated with G24.47 within the circle shown in (c). The ZAMS loci, with the spectral types indicated, are drawn for 0, 10, 20, and 30 magnitudes of visual extinction corrected for the distance. The parallel lines are the reddening vectors for the spectral types. Stars earlier than spectral type B3 are shown as stars. (b) The color–color diagram for the 23 sources earlier than B3. The loci of giants and main-sequence stars, taken from Koornneef (1983) and Bessell & Brett (1988), are shown as black and green curves, respectively. The dashed line shows the locus of the Herbig AeBe stars adopted from Lada & Adams (1992). The locus of classical T Tauri (Meyer et al. 1997) is shown as a dashed–dotted line. The parallel lines are the reddening vectors where the ones corresponding to M4, B3, and O5 are shown as dotted lines. The cross marks indicate intervals of 5 mag of visual extinction. Sources (E1–E12) within the reddening vectors of B3 and O5 are labeled in panels (a) and (b). Both plots are in the Bessell & Brett (1988) system. (c) The color scale shows the VLA 4.86 GHz map of the region associated with G24.47 with contour levels at [3, 7, 20, 35, 50, 70, 90, 100, 110, 120, 135] × σ (σ = 0.4 mJy beam^{-1}). The crosses represent the central positions of the VLA cores. The positions of the sources E1–E12 are indicated. The ellipse at the bottom left shows the beam.

Table D1
Candidate Ionizing Sources

Source	Coordinates		J	H	K
	R.A. (J2000)	Decl. (J2000)	(mag)	(mag)	(mag)
E1[a]	18:34:10.55	−7:18:14.80	15.748	14.563	13.878
E2[b]	18:34:10.49	−7:18:00.37	13.021	11.853	11.135
E3[b]	18:34:10.37	−7:17:53.11	13.771	12.313	11.489
E4[b]	18:34:10.26	−7:17:58.62	14.555	12.966	11.852
E5[a]	18:34:09.98	−7:18:16.60	14.265	13.291	12.683
E6[a]	18:34:09.91	−7:18:04.12	14.602	13.586	12.833
E7[a]	18:34:09.52	−7:18:06.55	13.984	13.030	12.401
E8[b]	18:34:09.32	−7:18:09.18	11.547	10.356	9.603
E9[a]	18:34:09.31	−7:17:45.66	14.634	13.263	12.456
E10[a]	18:34:09.22	−7:17:56.34	15.592	14.503	13.879
E11[a]	18:34:09.02	−7:17:59.67	16.188	14.521	13.525
E12[a]	18:34:08.75	−7:18:06.21	16.338	14.260	13.101

Notes.
[a] Value from the UKIDSS catalog.
[b] Value from the 2MASS catalog.

Appendix E
Initial Particle Number Density

The particle number density, n_0, is obtained by estimating the mass of the material within the ionized ring (radius of ∼0.8 pc). For this, we used the ATLASGAL 870 μm map for the region associated with G24.47. The mass, M, is given by

$$M = \frac{F_\nu\, d^2\, R_{\rm gd}}{B_\nu(T_{\rm d})\,\kappa_\nu}, \tag{E1}$$

where F_ν is the integrated 870 μm flux density; d is the distance to the source; $R_{\rm gd}$ is the gas-to-dust ratio taken as 100; B_ν is the Planck function at dust temperature $T_{\rm d}$ taken as 30.4 K (Liu et al. 2020); and κ_ν is the dust opacity coefficient taken to be 1.85 $\rm cm^2\,g^{-1}$ (Urquhart et al. 2018). This gives a mass estimate of 1409 $M_\odot$ and particle number density of $n_0 \sim 10^4\ \rm cm^{-3}$.

ORCID iDs

Anindya Saha https://orcid.org/0000-0002-9793-3039
Anandmayee Tej https://orcid.org/0000-0001-5917-5751
Hong-Li Liu https://orcid.org/0000-0003-3343-9645
Tie Liu https://orcid.org/0000-0002-5286-2564
Paul F. Goldsmith https://orcid.org/0000-0002-6622-8396
Chang Won Lee https://orcid.org/0000-0002-3179-6334
Jinhua He https://orcid.org/0000-0002-3938-4393
Mika Juvela https://orcid.org/0000-0002-5809-4834
Leonardo Bronfman https://orcid.org/0000-0002-9574-8454
Tapas Baug https://orcid.org/0000-0003-0295-6586
Enrique Vázquez-Semadeni https://orcid.org/0000-0002-1424-3543
Patricio Sanhueza https://orcid.org/0000-0002-7125-7685
Shanghuo Li https://orcid.org/0000-0003-1275-5251
James O. Chibueze https://orcid.org/0000-0002-9875-7436
N. K. Bhadari https://orcid.org/0000-0001-8812-8460
Lokesh K. Dewangan https://orcid.org/0000-0001-6725-0483
Swagat Ranjan Das https://orcid.org/0000-0002-3658-0516
Feng-Wei Xu https://orcid.org/0000-0001-5950-1932
Namitha Issac https://orcid.org/0000-0002-7881-689X
Jihye Hwang https://orcid.org/0000-0001-7866-2686
L. Viktor Tóth https://orcid.org/0000-0002-5310-4212

References

Arce, H. G., Borkin, M. A., Goodman, A. A., Pineda, J. E., & Beaumont, C. N. 2011, ApJ, 742, 105
Areal, M. B., Buccino, A., Paron, S., Fariña, C., & Ortega, M. E. 2020, MNRAS, 496, 870
Astropy Collaboration, Price-Whelan, A. M., Sipőcz, B. M., et al. 2018, AJ, 156, 123
Beaumont, C. N., & Williams, J. P. 2010, ApJ, 709, 791
Becker, R. H., White, R. L., Helfand, D. J., & Zoonematkermani, S. 1994, ApJS, 91, 347
Benjamin, R. A., Churchwell, E., Babler, B. L., et al. 2003, PASP, 115, 953
Bertoldi, F., & McKee, C. F. 1992, ApJ, 395, 140
Bessell, M. S., & Brett, J. M. 1988, PASP, 100, 1134
Bhadari, N. K., Dewangan, L. K., Zemlyanukha, P. M., et al. 2021, ApJ, 922, 207
Bonne, L., Kabanovic, S., Schneider, N., et al. 2023, A&A, 679, L5
Cambrésy, L., Marton, G., Feher, O., Tóth, L. V., & Schneider, N. 2013, A&A, 557, A29
Churchwell, E. 2002, ARA&A, 40, 27
Churchwell, E., Povich, M. S., Allen, D., et al. 2006, ApJ, 649, 759
Churchwell, E., Walmsley, C. M., & Cesaroni, R. 1990, A&AS, 83, 119
Contreras, Y., Garay, G., Rathborne, J. M., & Sanhueza, P. 2016, MNRAS, 456, 2041
Dale, J. E., Haworth, T. J., & Bressert, E. 2015, MNRAS, 450, 1199
Das, S. R., Tej, A., Vig, S., et al. 2017, MNRAS, 472, 4750
Davies, B., Hoare, M. G., Lumsden, S. L., et al. 2011, MNRAS, 416, 972
de la Fuente, E., Tafoya, D., Trinidad, M. A., et al. 2020, MNRAS, 497, 4436
Deharveng, L., Lefloch, B., Zavagno, A., et al. 2003, A&A, 408, L25
Deharveng, L., Schuller, F., Anderson, L. D., et al. 2010, A&A, 523, A6
Dyson, J. E., & Williams, D. A. 1980, Physics of the Interstellar Medium (Manchester: Manchester Univ. Press)
Elmegreen, B. G., & Lada, C. J. 1977, ApJ, 214, 725
Figueira, M., Zavagno, A., Deharveng, L., et al. 2017, A&A, 600, A93
Garay, G., Rodriguez, L. F., Moran, J. M., & Churchwell, E. 1993, ApJ, 418, 368
González-Samaniego, A., & Vazquez-Semadeni, E. 2020, MNRAS, 499, 668
Haid, S., Walch, S., Seifried, D., et al. 2018, MNRAS, 478, 4799
Herschel Point Source Catalogue Working Group, Marton, G., Calzoletti, L., et al. 2020, yCat, VIII/106
Hoare, M. G., Kurtz, S. E., Lizano, S., Keto, E., & Hofner, P. 2007, in Protostars and Planets V, ed. B. Reipurth, D. Jewitt, & K. Keil (Tucson, AZ: Univ, of Arizona Press), 181
Hoq, S., Jackson, J. M., Foster, J. B., et al. 2013, ApJ, 777, 157
Hunter, T. R., Brogan, C. L., Indebetouw, R., & Cyganowski, C. J. 2008, ApJ, 680, 1271
Kabanovic, S., Schneider, N., Ossenkopf-Okada, V., et al. 2022, A&A, 659, A36
Kalcheva, I. E., Hoare, M. G., Urquhart, J. S., et al. 2018, A&A, 615, A103
Kauffmann, J., Pillai, T., & Goldsmith, P. F. 2013, ApJ, 779, 185
Kendrew, S., Simpson, R., Bressert, E., et al. 2012, ApJ, 755, 71
Keto, E., Zhang, Q., & Kurtz, S. 2008, ApJ, 672, 423
Koornneef, J. 1983, A&A, 128, 84
Kurtz, S. 2005, in IAU Symp. 227, Massive Star Birth: A Crossroads of Astrophysics, ed. R. Cesaroni et al. (Cambridge: Cambridge Univ. Press), 111
Kwan, J. 1997, ApJ, 489, 284
Lada, C. J., & Adams, F. C. 1992, ApJ, 393, 278
Lawrence, A., Warren, S. J., Almaini, O., et al. 2007, MNRAS, 379, 1599
Li, C.-X., Wang, H.-C., Ma, Y.-H., et al. 2022, RAA, 22, 045008
Li, S., Zhang, Q., Liu, H. B., et al. 2020, ApJ, 896, 110
Liu, H.-L., Li, J.-Z., Wu, Y., et al. 2016, ApJ, 818, 95
Liu, H.-L., Liu, T., Evans, N. J. I., et al. 2021, MNRAS, 505, 2801
Liu, H.-L., Tej, A., Liu, T., et al. 2022, MNRAS, 510, 5009

Liu, H.-L., Tej, A., Liu, T., et al. 2023, MNRAS, 522, 3719
Liu, T., Evans, N. J., Kim, K.-T., et al. 2020, MNRAS, 496, 2790
Liu, X., Liu, T., Zhu, L., et al. 2024, RAA, 24, 025009
Lockman, F. J. 1989, ApJS, 71, 469
Lucas, P. W., Hoare, M. G., Longmore, A., et al. 2008, MNRAS, 391, 136
Luisi, M., Anderson, L. D., Schneider, N., et al. 2021, SciA, 7, eabe9511
Mac Low, M.-M., Toraskar, J., Oishi, J. S., & Abel, T. 2007, ApJ, 668, 980
Martín-Hernández, N. L., Vermeij, R., & van der Hulst, J. M. 2005, A&A, 433, 205
Martins, F., & Palacios, A. 2017, A&A, 598, A56
Mayya, Y. D., Alzate, J. A., Lomelí-Núez, L., et al. 2023, MNRAS, 521, 5492
Meyer, M. R., Calvet, N., & Hillenbrand, L. A. 1997, AJ, 114, 288
Oey, M. S., Watson, A. M., Kern, K., & Walth, G. L. 2005, AJ, 129, 393
Pabst, C., Higgins, R., Goicoechea, J. R., et al. 2019, Natur, 565, 618
Panagia, N. 1973, AJ, 78, 929
Paron, S., Petriella, A., & Ortega, M. E. 2011, A&A, 525, A132
Patel, A. L., Urquhart, J. S., Yang, A. Y., et al. 2023, MNRAS, 524, 4384
Potdar, A., Das, S. R., Issac, N., et al. 2022, MNRAS, 510, 658
Purcell, C. R., Hoare, M. G., Cotton, W. D., et al. 2013, ApJS, 205, 1
Purcell, C. R., Minier, V., Longmore, S. N., et al. 2009, A&A, 504, 139
Quireza, C., Rood, R. T., Bania, T. M., Balser, D. S., & Maciel, W. J. 2006, ApJ, 653, 1226
Rosolowsky, E. W., Pineda, J. E., Kauffmann, J., & Goodman, A. A. 2008, ApJ, 679, 1338
Saha, A., Tej, A., Liu, H.-L., et al. 2022, MNRAS, 516, 1983
Sanhueza, P., Contreras, Y., Wu, B., et al. 2019, ApJ, 886, 102
Sanhueza, P., Jackson, J. M., Foster, J. B., et al. 2012, ApJ, 756, 60
Saral, G., Hora, J. L., Audard, M., et al. 2017, ApJ, 839, 108
Schlingman, W. M., Shirley, Y. L., Schenk, D. E., et al. 2011, ApJS, 195, 14
Schmiedeke, A., Schilke, P., Möller, T., et al. 2016, A&A, 588, A143
Skrutskie, M. F., Cutri, R. M., Stiening, R., et al. 2006, AJ, 131, 1163
Stutz, A. M., Tobin, J. J., Stanke, T., et al. 2013, ApJ, 767, 36
Tang, Y.-W., Koch, P. M., Peretto, N., et al. 2019, ApJ, 878, 10
Thompson, M. A., Urquhart, J. S., Moore, T. J. T., & Morgan, L. K. 2012, MNRAS, 421, 408
Urquhart, J. S., König, C., Giannetti, A., et al. 2018, MNRAS, 473, 1059
Urquhart, J. S., Moore, T. J. T., Csengeri, T., et al. 2014, MNRAS, 443, 1555
Urquhart, J. S., Wells, M. R. A., Pillai, T., et al. 2022, MNRAS, 510, 3389
Walch, S. K., Whitworth, A. P., Bisbas, T., Wünsch, R., & Hubber, D. 2012, MNRAS, 427, 625
Walsh, A. J., Burton, M. G., Hyland, A. R., & Robinson, G. 1998, MNRAS, 301, 640
Wang, Y., Audard, M., Fontani, F., et al. 2016, A&A, 587, A69
Watson, C., Povich, M. S., Churchwell, E. B., et al. 2008, ApJ, 681, 1341
Wink, J. E., Altenhoff, W. J., & Mezger, P. G. 1982, A&A, 108, 227
Xu, F.-W., Wang, K., Liu, T., et al. 2023, MNRAS, 520, 3259
Xu, J.-L., Xu, Y., Zhang, C.-P., et al. 2018, A&A, 609, A43
Yang, A. Y., Thompson, M. A., Tian, W. W., et al. 2019, MNRAS, 482, 2681
Yang, A. Y., Urquhart, J. S., Thompson, M. A., et al. 2021, A&A, 645, A110
Zavagno, A., Deharveng, L., Comerón, F., et al. 2006, A&A, 446, 171
Zavagno, A., Pomarès, M., Deharveng, L., et al. 2007, A&A, 472, 835
Zhang, C., Zhu, F.-Y., Liu, T., et al. 2023a, MNRAS, 520, 3245
Zhang, S., Wang, K., Liu, T., et al. 2023b, MNRAS, 520, 322